

---

# RESTRICTED BOLTZMANN MACHINE REPRESENTATION FOR THE GROUNDSTATE AND EXCITED STATES OF KITAEV HONEYCOMB MODEL

---

A PREPRINT

**Mohammadreza Noormandipour<sup>\*,a</sup>, Youran Sun<sup>†,b,c</sup>, Babak Haghighat<sup>‡,b</sup>**  
<sup>a</sup> *DAMTP, University of Cambridge, Wilberforce Road, Cambridge CB3 0WA, UK*  
<sup>b</sup> *Yau Mathematical Sciences Center, Tsinghua University, Beijing, 100084, China*  
<sup>c</sup> *School of Physics, Peking University, Beijing, China*

March 14, 2020

## ABSTRACT

In this work, the capability of restricted Boltzmann machines (RBMs) to find solutions for the Kitaev honeycomb model is investigated. The measured groundstate (GS) energy of the system is compared and shown to reside within less than 5% error of the analytically derived value of the energy. Moreover, given a set of single shot measurements of exact solutions of the model, an RBM is used to perform quantum state tomography and the obtained result has a 97% overlap with the exact analytic result. Furthermore, the possibility of realizing anyons in the RBM is discussed and an algorithm is given to build these anyonic excitations and braid them as a proof of concept for performing quantum gates and doing quantum computation.

**Keywords** Restricted Boltzmann Machine (RBM) · Feed-Forward Neural Network (FFNN) · Honeycomb Lattice Model · Quantum State Tomography (QST) · Topological Phases of Matter · Anyons · Quantum Computing

## 1 Introduction

The Honeycomb model is a 2-dimensional lattice spin system (see Fig.1) which was first introduced by Kitaev in 2006 [1] and is famous because of the topological quantum order due to a degenerate gapped groundstate which is persistent to local and finite-sized perturbations. The system also supports both abelian and non-abelian topological phases as demonstrated in the original proposal [1]. There is a wide range of applications for this model, from fault-tolerant quantum computation [2] to analytical study of strongly correlated systems [3] and quantum spin liquids [4]. The honeycomb lattice is not a Bravais lattice in its original structure, but it can be considered as a triangular Bravais lattice with a two-spin basis. The direct Bravais lattice and the primitive cells are illustrated in Fig. 1a with the dashed lines. Each primitive cell has a pair of odd and even indexed spins. Just for the sake of simplicity we will denote each cell with the even indexed (empty circles) spins of the system. The primitive vectors of the lattice,  $\mathbf{a}_1$  and  $\mathbf{a}_2$  are also shown in Fig. 1a (see also Equ. 1). The entire lattice can be tiled and covered with primitive cells using translations composed of different linear combinations of primitive vectors.

$$\mathbf{a}_1 = \sqrt{3}a\mathbf{e}_x \quad \& \quad \mathbf{a}_2 = \frac{\sqrt{3}}{2}a(\mathbf{e}_x, \sqrt{3}\mathbf{e}_y) \quad (1)$$

---

<sup>\*</sup>mrn31@cam.ac.uk

<sup>†</sup>syouran0508@gmail.com

<sup>‡</sup>babakhaghighat@tsinghua.edu.cn

Where  $a$  is the lattice constant. The reciprocal lattice for the triangle lattice can be obtained by solving Equ.2 for basis vectors of the reciprocal lattice,  $\mathbf{b}_1$  and  $\mathbf{b}_2$ .

$$\mathbf{a}_i \cdot \mathbf{b}_j = 2\pi\delta_{ij} \quad (2)$$

The solution is as below:

$$\mathbf{b}_1 = \frac{2\pi}{\sqrt{3}a}(\mathbf{e}_x - \frac{1}{\sqrt{3}}\mathbf{e}_y) \quad \& \quad \mathbf{b}_2 = \frac{4\pi}{3a}\mathbf{e}_y \quad (3)$$

The reciprocal lattice is depicted in Fig. 1b.

The Hamiltonian of the Kitaev model is a nearest-neighbor interaction of Pauli matrices on a honeycomb lattice as written in Equ.4, where  $r$  &  $r'$  are indices for the nearest neighbour spins. The physics of the system is symmetric under permutation of coupling strengths  $J_\alpha$  with  $\alpha = x, y, z$  and due to an-isotropic interaction the model is a frustrated spin system, because a spin cannot satisfy conflicting demands of orientation from its three neighboring sites [1].

$$H = - \sum_{\alpha} J_{\alpha} \sum_{\alpha-bonds} \sigma_r^{\alpha} \sigma_{r'}^{\alpha} \quad (4)$$

In this paper we apply the approach developed in [5] to the Honeycomb model. In Section2, we briefly review the analytical solution of the model. In Section3 the mapping of the spin model to an RBM architecture is explained. In particular, we demonstrate how to calculate the groundstate and excited states of the Honeycomb model using machine learning techniques. To this end we employ the NetKet environment [6] to train a restricted Boltzmann machine (RBM) in order to find a groundstate via gradient descent. In Section4 realization of vortices is discussed from both analytical and RBM language points of view. In brief, a vortex pair can be created by adjusting the parameters of the RBM and subsequent braiding can be achieved by further adjustments of parameters. Section5 is dedicated to results and relevant discussions and finally we conclude in Section6. An important application of the techniques developed in this paper is the reconstruction of a given quantum state from simple measurements known as quantum state tomography [7].

## 2 Solution of the Model

In this section an exact solution of the system is provided and an explicit form of the groundstate energy is achieved where we will be following references [1, 8, 9]. First of all, we fermionize the Hamiltonian by performing a one-dimensional Jordan-Wigner transformation [10] defined in Equ.5. A deformation of the hexagonal lattice to a brick-wall lattice (see Fig. 2) clarifies the mechanism of the Jordan-Wigner transformation and why it is one-dimensional [11]. In the brick-wall lattice, each lattice site  $r$  is denoted by the coordinates  $(i, j)$ .

$$\begin{aligned} \sigma_{i,j}^+ &= 2[\prod_{j' < j} \prod_{i'} \sigma_{i',j'}^z][\prod_{i' < i} \sigma_{i',j}^z]a_{i,j}^{\dagger} \\ \sigma_{i,j}^- &= 2[\prod_{j' < j} \prod_{i'} \sigma_{i',j'}^z][\prod_{i' < i} \sigma_{i',j}^z]a_{i,j} \\ \sigma_{i,j}^z &= 2a_{i,j}^{\dagger}a_{i,j} - 1 \end{aligned} \quad (5)$$

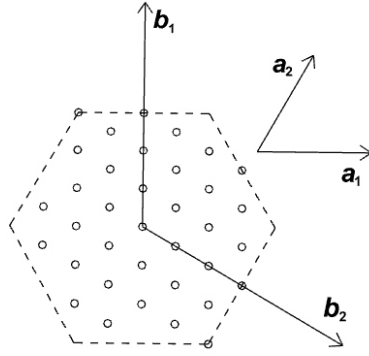
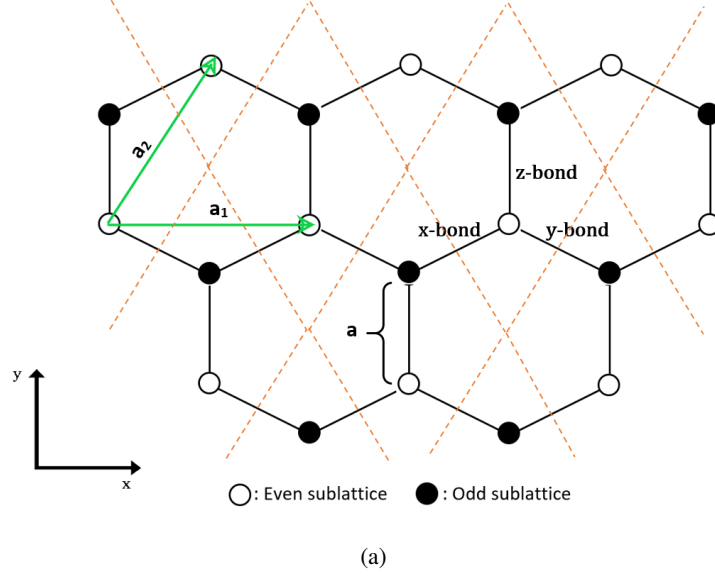


Figure 1: (a) The honeycomb lattice in position space and its primitive vectors and primitive cell. (b) First Brillouin zone and primitive vectors of reciprocal lattice.

This transformation maps the Hilbert space of spins to the Hilbert space of spinless complex fermions. Using the fact that  $\sigma^\pm = \sigma^x \pm i\sigma^y$  one can expand the Hamiltonian in Equ.4 into three terms and rewrite them as below [9].

$$\begin{aligned}
 \sigma_{i,j}^x \sigma_{i+1,j}^x &= \prod_{i' < i} \sigma_{i',j}^z (a_{i,j}^\dagger + a_{i,j}) \prod_{i' < i+1} \sigma_{i',j}^z (a_{i+1,j}^\dagger + a_{i+1,j}) \\
 &= (a_{i,j}^\dagger + a_{i,j}) \sigma_{i,j}^z (a_{i+1,j}^\dagger + a_{i+1,j}) \\
 &= -(a_{i,j}^\dagger - a_{i,j}) (a_{i+1,j}^\dagger + a_{i+1,j}) \\
 \sigma_{i,j}^y \sigma_{i+1,j}^y &= - \prod_{i' < i-1} \sigma_{i',j}^z (a_{i-1,j}^\dagger - a_{i-1,j}) \prod_{i' < i} \sigma_{i',j}^z (a_{i,j}^\dagger - a_{i,j}) \\
 &= -(a_{i-1,j}^\dagger - a_{i-1,j}) \sigma_{i-1,j}^z (a_{i,j}^\dagger - a_{i,j}) \\
 &= (a_{i-1,j}^\dagger + a_{i-1,j}) (a_{i,j}^\dagger - a_{i,j}) \\
 \sigma_{i,j}^z \sigma_{i,j+1}^z &= (2a_{i,j}^\dagger a_{i,j} - 1)(2a_{i,j+1}^\dagger a_{i,j+1} - 1)
 \end{aligned} \tag{6}$$

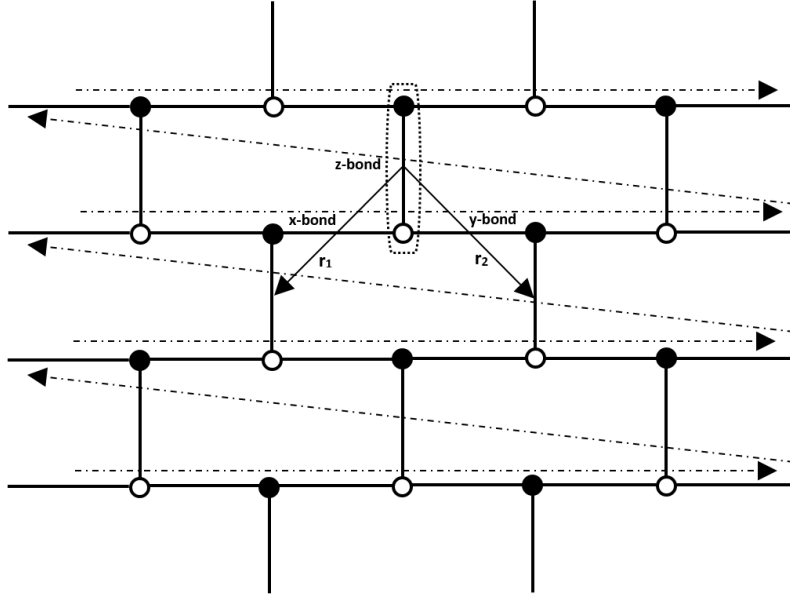


Figure 2: Brick-wall lattice and the Jordan-Wigner transformation path depicted with the dashed arrows. The  $\mathbf{r}_1$  and  $\mathbf{r}_2$  are the primitive vectors for this lattice.

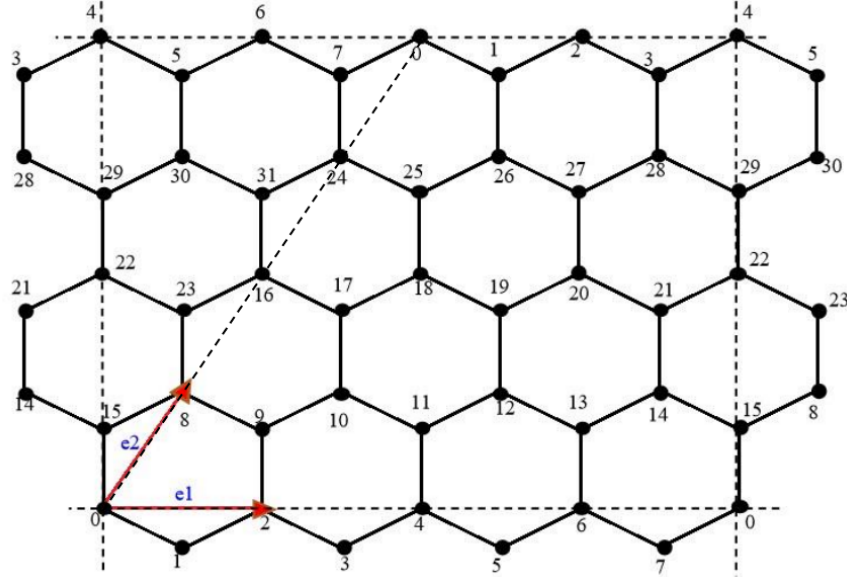


Figure 3: Kitaev Honeycomb lattice model on a torus: The generators of the lattice in position space are named  $\mathbf{e}_1$  and  $\mathbf{e}_2$ , as shown in the image above. Hence, the lattice points are  $\mathbf{L} = n_1\mathbf{e}_1 + n_2\mathbf{e}_2$  with  $n_1, n_2 \in \mathbb{Z}$  and the above lattice is drawn for  $N_1 = N_2 = 4$  with toric boundary conditions.

Therefore, the Hamiltonian transforms to the one in Equ.7.

$$\begin{aligned}
 H = & + J_x \sum_{x-links} (a_{i,j}^\dagger - a_{i,j})(a_{i+1,j}^\dagger + a_{i+1,j}) \\
 & - J_y \sum_{y-links} (a_{i-1,j}^\dagger + a_{i-1,j})(a_{i,j}^\dagger - a_{i,j}) \\
 & - J_z \sum_{z-links} (2a_{i,j}^\dagger a_{i,j} - 1)(2a_{i,j+1}^\dagger a_{i,j+1} - 1)
 \end{aligned} \tag{7}$$

The  $J_x$  and  $J_y$  terms are quadratic interactions in spinless fermions and are easy to solve, however, the  $J_z$  term is a product of number density operators and can be further simplified by introducing the Majorana operators in Equ.8 [9]. As we will see, this simplification can be done due to the presence of the conserved quantity called plaquette operator  $B_p$  [9].

$$\begin{aligned} c_{i,j} &= i(a_{i,j}^\dagger - a_{i,j}) \quad , \quad d_{i,j} = a_{i,j}^\dagger + a_{i,j} \quad , \quad \text{for } i+j = \text{even} \equiv \circ \\ c_{i,j} &= a_{i,j}^\dagger + a_{i,j} \quad , \quad d_{i,j} = i(a_{i,j}^\dagger - a_{i,j}) \quad , \quad \text{for } i+j = \text{odd} \equiv \bullet \end{aligned} \quad (8)$$

These operators have the following commutation relations:

$$\begin{aligned} c_{i,j}^2 &= d_{i,j}^2 = 1 \\ \{c_{i,j}, c_{i',j'}\} &= \{d_{i,j}, d_{i',j'}\} = 2\delta_{ii'}\delta_{jj'} \\ \{c_{i,j}, d_{i',j'}\} &= 0 \end{aligned} \quad (9)$$

Then, the  $J_z$  term can be rewritten using the Majorana operators:

$$\begin{aligned} \sigma_{i,j}^z \sigma_{i,j+1}^z &= (2a_{i,j}^\dagger a_{i,j} - 1)(2a_{i,j+1}^\dagger a_{i,j+1} - 1) \\ &= i(id_{i,j+1} d_{i,j}) c_{i,j+1} c_{i,j} \end{aligned} \quad (10)$$

Finally, using the circle indices for the odd and even lattice sites as defined in Equ.8 the Hamiltonian transforms to the expression in Equ.11.

$$\begin{aligned} H &= -iJ_x \sum_{x\text{-links}} c_\circ c_\bullet \\ &\quad + iJ_y \sum_{y\text{-links}} c_\bullet c_\circ \\ &\quad - iJ_z \sum_{z\text{-links}} (id_\bullet d_\circ) c_\bullet c_\circ \end{aligned} \quad (11)$$

If we write the Hamiltonian as a sum over unit cells we have:

$$H = i \sum_{\mathbf{r}} [J_x c_{\bullet, \mathbf{r}} c_{\circ, \mathbf{r}+\mathbf{r}_1} + J_y c_{\bullet, \mathbf{r}} c_{\circ, \mathbf{r}+\mathbf{r}_2} - J_z (id_{\bullet, \mathbf{r}} d_{\circ, \mathbf{r}}) c_{\bullet, \mathbf{r}} c_{\circ, \mathbf{r}}] \quad (12)$$

where  $\mathbf{r}$  is the position vector of z-bonds or unit cells (see Fig.2). It makes no difference in the physics if we set  $\mathbf{r}$  to be any point along the z-bond, whether we choose an even site or an odd site or some point in the middle, they are all related through translation. What will be important in what follows, is that now since we have grouped a pair of even and odd sites as an unit cell, to evaluate the summation over the unit cells, it is sufficient to just run over the even or odd sites.

Furthermore, the  $\alpha_{\mathbf{r}} = (id_{\bullet, \mathbf{r}} d_{\circ, \mathbf{r}})$  operators are defined on each z-bond of the lattice (labeled by  $\mathbf{r}$ ) and they commute with the Hamiltonian and are good quantum numbers. Moreover, it can easily be shown that each plaquette operator can be written as:

$$B_p = \sigma_1^y \sigma_2^z \sigma_3^x \sigma_4^y \sigma_5^z \sigma_6^x = \alpha_{61} \alpha_{43} \quad (13)$$

On the other hand, from Lieb's theorem [12] we know that the groundstate manifold is obtained by setting  $B_p = 1, \forall p$ . Thus the uniform choice of  $\alpha_{\mathbf{r}} = 1, \forall \mathbf{r}$  corresponds to a vortex-free sector, nevertheless all configurations leading to the same sector are equivalent.

We also introduce a Dirac fermion on each z-link using the Majorana operators:

$$\begin{aligned} d_{\mathbf{r}} &= \frac{1}{2}(c_{\bullet, \mathbf{r}} - ic_{\circ, \mathbf{r}}) \\ d_{\mathbf{r}}^{\dagger} &= \frac{1}{2}(c_{\bullet, \mathbf{r}} + ic_{\circ, \mathbf{r}}) \end{aligned} \quad (14)$$

Using the inverse transformation we can rewrite the Hamiltonian:

$$\begin{aligned} H &= \sum_{\mathbf{r}} [J_x(d_{\mathbf{r}}^{\dagger} + d_{\mathbf{r}})(d_{\mathbf{r}+\mathbf{r}_1}^{\dagger} - d_{\mathbf{r}+\mathbf{r}_1}) \\ &\quad + J_y(d_{\mathbf{r}}^{\dagger} + d_{\mathbf{r}})(d_{\mathbf{r}+\mathbf{r}_2}^{\dagger} - d_{\mathbf{r}+\mathbf{r}_2}) \\ &\quad + J_z\alpha_{\mathbf{r}}(2d_{\mathbf{r}}^{\dagger}d_{\mathbf{r}} - 1)] \end{aligned} \quad (15)$$

The Hamiltonian is translation invariant and can be transformed to momentum space in order to be diagonalized. We define the Fourier transform for the Dirac fermion through:

$$\begin{aligned} d_{\mathbf{r}} &= \frac{1}{\sqrt{N}} \sum_{\mathbf{k}} e^{+i\mathbf{k} \cdot \mathbf{r}} d_{\mathbf{k}} \\ d_{\mathbf{r}}^{\dagger} &= \frac{1}{\sqrt{N}} \sum_{\mathbf{k}} e^{-i\mathbf{k} \cdot \mathbf{r}} d_{\mathbf{k}}^{\dagger} \end{aligned} \quad (16)$$

Setting  $\mathbf{k} \rightarrow -\mathbf{k}$  in  $d_{\mathbf{r}}^{\dagger}$  simplifies the calculations. We then have:

$$\begin{aligned} \mathbf{X} : & J_x \frac{1}{N} \sum_{\mathbf{r}} \sum_{\mathbf{k}, \mathbf{k}'} e^{+i\mathbf{k} \cdot \mathbf{r}} e^{+i\mathbf{k}' \cdot (\mathbf{r}+\mathbf{r}_1)} (d_{-\mathbf{k}}^{\dagger} + d_{\mathbf{k}})(d_{-\mathbf{k}'}^{\dagger} - d_{\mathbf{k}'}) \\ &= J_x \sum_{\mathbf{k}} [-2 \cos(k_1) d_{\mathbf{k}}^{\dagger} d_{\mathbf{k}} + i \sin(k_1) (d_{\mathbf{k}}^{\dagger} d_{-\mathbf{k}} - h.c.)] \\ \mathbf{Y} : & J_y \frac{1}{N} \sum_{\mathbf{r}} \sum_{\mathbf{k}, \mathbf{k}'} e^{+i\mathbf{k} \cdot \mathbf{r}} e^{+i\mathbf{k}' \cdot (\mathbf{r}+\mathbf{r}_2)} (d_{-\mathbf{k}}^{\dagger} + d_{\mathbf{k}})(d_{-\mathbf{k}'}^{\dagger} - d_{\mathbf{k}'}) \\ &= J_y \sum_{\mathbf{k}} [-2 \cos(k_2) d_{\mathbf{k}}^{\dagger} d_{\mathbf{k}} + i \sin(k_2) (d_{\mathbf{k}}^{\dagger} d_{-\mathbf{k}} - h.c.)] \\ \mathbf{Z} : & J_z \frac{1}{N} \sum_{\mathbf{r}} \sum_{\mathbf{k}, \mathbf{k}'} e^{+i\mathbf{k} \cdot \mathbf{r}} e^{+i\mathbf{k}' \cdot \mathbf{r}} (2d_{-\mathbf{k}}^{\dagger} d_{\mathbf{k}'}^{\dagger} - 1) \\ &= J_z \sum_{\mathbf{k}} 2d_{\mathbf{k}}^{\dagger} d_{\mathbf{k}} - J_z N. \end{aligned} \quad (17)$$

For the above equation we used the orthogonality relation in Fourier transformation:

$$\sum_{\mathbf{r}} e^{i(\mathbf{k}+\mathbf{k}') \cdot \mathbf{r}} = N\delta(\mathbf{k} + \mathbf{k}') \quad (18)$$

Using all previous transformations we obtain a Hamiltonian which is quadratic in the Dirac fermions living on each of the unit cells along the z-links:

$$\begin{aligned}
 H &= \sum_{\mathbf{k}} [\epsilon_{\mathbf{k}} d_{\mathbf{k}}^{\dagger} d_{\mathbf{k}} + \frac{1}{2} (i \Delta_{\mathbf{k}} d_{\mathbf{k}}^{\dagger} d_{-\mathbf{k}}^{\dagger} - i \Delta_{\mathbf{k}} d_{-\mathbf{k}} d_{\mathbf{k}})] - J_z N \\
 \epsilon_{\mathbf{k}} &= 2[J_z - J_x \cos(k_1) - J_y \cos(k_2)] \\
 \Delta_{\mathbf{k}} &= 2[J_x \sin(k_1) + J_y \sin(k_2)]
 \end{aligned} \tag{19}$$

By applying a unitary Bogoliubov transformation, we diagonalize the Hamiltonian which can be written as:

$$\begin{aligned}
 H &= \sum_{\mathbf{k}} \frac{1}{2} \begin{pmatrix} \gamma_{\mathbf{k}}^{\dagger} & \gamma_{-\mathbf{k}} \end{pmatrix} \begin{pmatrix} E_{\mathbf{k}} & 0 \\ 0 & -E_{\mathbf{k}} \end{pmatrix} \begin{pmatrix} \gamma_{\mathbf{k}} \\ \gamma_{-\mathbf{k}}^{\dagger} \end{pmatrix} \\
 &= \sum_{\mathbf{k}} E_{\mathbf{k}} \left( \gamma_{\mathbf{k}}^{\dagger} \gamma_{\mathbf{k}} - \frac{1}{2} \right), \quad E_{\mathbf{k}} = \sqrt{\epsilon_{\mathbf{k}}^2 + \Delta_{\mathbf{k}}^2},
 \end{aligned} \tag{20}$$

where  $\gamma_{\mathbf{k}}^{\dagger}$  and  $\gamma_{\mathbf{k}}$  are quasiparticle creation and annihilation operators. The groundstate energy can easily be read off from the above Hamiltonian and is given by  $E_{GS} = -\sum_{\mathbf{k}} \frac{E_{\mathbf{k}}}{2}$ .

### 3 Restricted Boltzmann Machine Representations

#### 3.1 RBM as a Neural Network Quantum State

With the ever growing applications of neural networks in sciences and the emergent new technologies to deploy and build physical neural networks, this is the right time to investigate potential applications of them in condensed matter systems. Recently, a new approach has been proposed for simulating topological quantum states using neural networks [5]. In this section we use the same approach to map the Honeycomb Kitaev model to a restricted Boltzmann machine (RBM). There are many reasons why an RBM is chosen. This particular architecture has proved to be effective in many tasks such as dimensional reduction, classification, regression, collaborative filtering, feature learning and topic modeling and moreover a general theorem shows that RBMs are universal approximators of discrete distributions [13].

Having a set of spins on a lattice,  $\Xi = (\sigma_1, \sigma_2, \dots, \sigma_N)$  (in our case the Jordan-Wigner chain of spins), our goal is to use an RBM to reduce the dimensionality of the Hilbert space and estimate the energy of the system in both groundstate and excited states to be able to classify different topological phases of the model. An RBM is a short range feed-forward neural network with two layers. The first layer (visible layer) has  $N$  nodes which are representing the physical spins in the Hamiltonian and the second layer (hidden layer) has  $M$  binary valued nodes (architecture of the network is shown in Fig.4).

The quantum state of the Honeycomb model, up to an irrelevant normalization factor, can be written as

$$|\Phi\rangle = \sum_{\Xi} \Phi_M(\Xi; \Omega) |\Xi\rangle \tag{21}$$

where

$$\begin{aligned}
 \Phi_M(\Xi; \Omega) &= \sum_{\{h_k\}} e^{\sum_k a_k \sigma_k^z + \sum_{k'} b_{k'} h_{k'} + \sum_{kk'} W_{kk'} h_k \sigma_k^z} \\
 &= e^{\sum_k a_k \sigma_k^z} \times \prod_{k'} \cosh \left( \sum_k W_{kk'} \sigma_k^z + b_{k'} \right)
 \end{aligned} \tag{22}$$

To obtain the second equality we used the values for  $\{h_k\} = \{-1, 1\}^M$  which is the set of possible configurations of hidden layer nodes and  $\Omega = (a_k, b_{k'}, W_{kk'})$  is the set of weights and biases of the RBM which should be trained in such

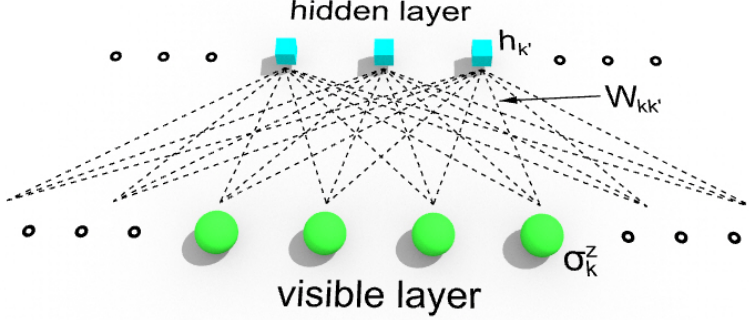


Figure 4: Fully connected Restricted Boltzmann machine architecture.

a way that the final RBM state represents the desired quantum state of the model (i.e. groundstate or the excited states). The combined number of weight and bias parameters and nodes is polynomial in system size and computationally feasible.

The mapping of the model to an RBM is done using the machinery already developed in the NetKet software package [6]. In order to train the network, the parameter space of the network was sampled using the Metropolis algorithm and the optimization iterations are based on the stochastic gradient descent algorithm.

### 3.2 Quantum State Tomography

Reconstruction of complex synthetic quantum states from experimental measurement data is computationally exponentially expensive. Therefore, the capability of neural network quantum states such as RBM to accurately and efficiently represent high-dimensional quantum states is beneficial to quantum state tomography. Apart from the numerous applications of QST, in our study case, the reconstructed states of the honeycomb model can later on be used for validation of particular quantum processes, e.g. braiding of vortices in the system, phase transitions, etc. at the experimental level and after implementation of the framework developed in Section 4. For instance, there are promising proposals for implementation of topological systems in cold atoms. A review has recently been published here [14].

In Section 5.3 we present QST results for the groundstate of a small system size of the honeycomb model, as proof of concept. In a normal QST task, the data sets come from experimental measurements, but since we don't have experimental data, we need to first find the exact wave-function for the system through exact diagonalization methods and then sample that wave-function by performing single shot measurements in different bases to build the data set.

After preparing the training data set, one needs to define a variational ansatz that should be trained on the measurement data. For the same motivations, we also choose an ansatz similar to the one used in [7]

$$\tilde{\psi}_{\lambda/\mu}(\sigma) = p_{\lambda}(\sigma) e^{i\phi_{\mu}(\sigma)} \quad (23)$$

where  $\phi_{\mu}(\sigma) = \log p_{\mu}(\sigma)$  and  $p_{\lambda/\mu}$  are RBM real probability distributions corresponding to two separate sets of RBM parameters  $\lambda/\mu$ . The probability distribution of single shot measurements in basis  $b$  is given by

$$P_b(\sigma) = |\langle \sigma | \hat{U}_b | \Psi_U \rangle|^2 \quad (24)$$

where  $|\Psi_U\rangle$  is the physical wave-function that we want to reconstruct.  $\hat{U}_b$  is the unitary transformation which rotates the wave-function to the basis  $b$  in which the measurement is performed. One can write the same expression for the probability distribution of the measurements for the variational wave-function  $|\tilde{\psi}_{\lambda/\mu}\rangle$ , namely  $\tilde{P}_b(\sigma)$ .



Then the QST problem reduces to a minimization task to find the set of parameters  $\kappa$  which minimizes the total Kullback-Leibler divergence between  $P_b(\sigma)$  and  $\tilde{P}_b(\sigma)$

$$\Xi(\kappa) = \sum_b \mathbb{KL}_b(\kappa) \quad (25)$$

where

$$\mathbb{KL}_b(\kappa) = \sum_{\sigma} P_b(\sigma) \log \frac{P_b(\sigma)}{\tilde{P}_b(\sigma)} \quad (26)$$

A more detailed explanation of how to perform this minimization using gradient descent can be found in [7]. In the present paper, we will follow the simpler approach of using the representation in Equ.21 (22) for the wave function, or in other words we work with a choice where  $\phi_{\mu}(\sigma) = 0$  while the RBM  $p_{\mu}(\sigma)$  has complex parameters and thus automatically takes care of the phase. The entire process of QST was implemented using NetKet [6] which has the above algorithm already built in.

## 4 Braiding

In this section we want to explore the possibility to create anionic excitations in the RBM representation and describe anyon braiding. Such a representation is important for various reasons, in particular for performing quantum computation [15].

First of all, let us describe the creation of these quasi-particles by starting with a groundstate sector and then subsequently changing the eigenvalue of the  $B_p$  operators from +1 to -1 locally and in the region where we want to realize the vortices in the system. In an arbitrary configuration of spins (not necessarily in the groundstate sector) it is easy to prove that  $\prod B_p = +1, \forall p$ . Hence, we can just build the vortices in pairs. For example, if you apply the operator  $\hat{O}_1$  to the groundstate, it produces two vortices in plaquettes 1 and 2 (see Fig.5) [16] .

$$\hat{O}_1 = \exp(-i\frac{\pi}{2}\hat{\sigma}_a^z) \quad (27)$$

Another possibility is to apply the following operator

$$\hat{O}_2 = \exp(-i\frac{\pi}{2}\hat{\sigma}_a^x) \exp(-i\frac{\pi}{2}\hat{\sigma}_b^y), \quad (28)$$

which produces two vortices along the  $\hat{z}$  direction in plaquettes 3 and 4.

The reason why these operators can produce vortices in the system can be explained by rewriting the Hamiltonian of the system in terms of Majorana fermions. Kitaev originally solved the Hamiltonian through this approach. The disadvantage of this approach in comparison to what was done above is that when the Hamiltonian is mapped to Majorana fermions, there are unphysical states in the system which need to be projected out. This will be clear as we go along.

We assume that there are two fermionic modes living on each lattice site corresponding to the four creation and annihilation operators  $a_{m,i}^{\dagger}$  and  $a_{m,i}$ , where  $m \in \{1, 2\}$  is the index for the modes and  $i$  is the index for the lattice sites. Here unlike before, we use one index for lattice site to avoid unnecessary complications. Then we will separate the imaginary and real parts of these operators, to define the Majorana fermions as below

$$\begin{aligned} c_i &= a_{1,i} + a_{1,i}^{\dagger} \\ b_i^x &= i(a_{1,i}^{\dagger} - a_{1,i}) \\ b_i^y &= a_{2,i} + a_{2,i}^{\dagger} \\ b_i^z &= i(a_{2,i}^{\dagger} - a_{2,i}) \end{aligned} \quad (29)$$

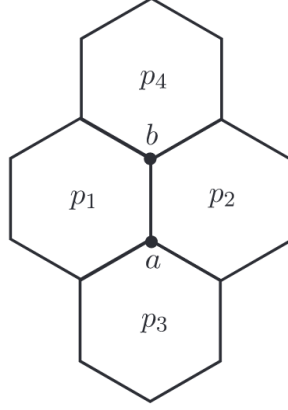


Figure 5: Demonstration of vortex pair realization using operators  $\hat{O}_{1,2}$ .

Notice that the spins have a two dimensional space (being up or down) and now that we are representing them with four Majorana modes (two complex fermionic modes), we need to project out the unphysical states. The Fock space of the complex fermionic modes can be represented as  $\{|00\rangle, |01\rangle, |10\rangle, |11\rangle\}$ . We make the following correspondence between the states of spins and fermions

$$\begin{aligned} |\uparrow\rangle &= |00\rangle \\ |\downarrow\rangle &= |11\rangle \end{aligned} \quad (30)$$

One can define the projector  $P_i$  on site  $i$  [17] to do this job for us

$$P_i = \frac{1 + D_i}{2} \quad \text{where} \quad D_i = (1 - 2a_{1,i}^\dagger a_{1,i})(1 - 2a_{2,i}^\dagger a_{2,i}) = b_i^x b_i^y b_i^z c_i. \quad (31)$$

One can easily show that the relation between Majorana operators and the original Pauli operators is as follows

$$\sigma_i^\alpha = i b_i^\alpha c_i \quad \text{for} \quad \alpha \in \{x, y, z\}. \quad (32)$$

In fact, by the above projection, we satisfied the extra condition coming from the algebra of Pauli matrices,  $-i\sigma_i^x \sigma_i^y \sigma_i^z = b_i^x b_i^y b_i^z c_i = \mathbb{1}$ . Therefore, the eigenvalue of the projector  $P_i$  for physical states is 1 and for unphysical states is 0.

Using Equ.32 the Hamiltonian can be written in terms of Majorana operators as

$$H = \frac{i}{2} \sum_{i,j} A_{ij} c_i c_j \quad \text{where} \quad A_{ij} = J_{ij} u_{ij} \quad \text{and} \quad u_{ij} = i b_i^\alpha b_j^\alpha \quad \text{with} \quad \alpha \in \{x, y, z\}. \quad (33)$$

The  $u_{ij}$  are antisymmetric Hermitian link operators with eigenvalues  $\pm 1$

$$u_{ij} = -u_{ji}, \quad u_{ij}^2 = 1, \quad u_{ij}^\dagger = u_{ij} \quad (34)$$

The link operators commute with the Hamiltonian,  $[H, u_{ij}] = 0$ , so they are local symmetries. In this form, the Hamiltonian is representing a tight binding model of free Majorana fermions hopping along the lattice, with tunneling couplings that depend on the eigenvalues of link operators which can be thought of as a classical  $\mathbb{Z}_2$  gauge field. One can assign a configuration  $\{u\}$  to all link operators and diagonalize the resulting quadratic Hamiltonian in Majorana operators directly and obtain the spectrum and groundstate energy for  $H\{u\}$ . But which configuration  $\{u\}$  corresponds to the global minimum of the energy? This question has been answered by Lieb (1994) [12]. The groundstate lies in the sector with  $B_p = 1 \ \forall p$  and since the  $B_p$  operators are the only gauge invariant objects, every gauge fixing choice  $\{u\}$  which leads to this particular configuration for  $B_p$  is equivalent. Therefore, our goal is to find a configuration  $\{u\}$  which leads to  $B_p = 1 \ \forall p$ .

Next, we define the vortex operator  $W_p$  as

$$W_p = \prod_{(i,j) \in \partial P} u_{ij} \quad \text{where} \quad \begin{cases} i \in \text{even sublattice} \\ j \in \text{odd sublattice} \end{cases} . \quad (35)$$

The vortex operator can be simplified as below

$$\begin{aligned} W_p &= u_{12}^x u_{32}^y u_{34}^z u_{54}^x u_{56}^y u_{16}^z \\ &= -(i)^6 c_1^x c_2^x c_2^y c_3^y c_3^z c_4^z c_4^x c_5^x c_5^y c_6^y c_6^z c_1^z \\ &= \sigma_1^y D_1 \sigma_2^z D_2 \sigma_3^x D_3 \sigma_4^y D_4 \sigma_5^z D_5 \sigma_6^x D_6 , \end{aligned} \quad (36)$$

where we used  $ic_j^x c_j^y = -\sigma_j^z D_j$  and cyclic permutations. Considering the fact that  $[W_p, H] = [W_p, D_i] = 0$ , in the physical subspace where  $D_j = 1$  we recover  $W_p = B_p$ . Therefore, the uniform choice of  $u_{ij} = 1$  for every link will lead us to the groundstate in the extended (not yet projected) space with  $B_p = 1$ . In order to find the physical groundstate, we apply the global projector  $\mathbf{D}$  to project out the unphysical states

$$|\psi_w\rangle_{\text{physical}} = \mathbf{D} |\psi_u\rangle_{\text{extended}}, \quad \text{where} \quad \mathbf{D} = \prod_{i=1}^N P_i \quad (37)$$

Now we are at a point to explain in detail why the operators  $\hat{O}_1$  and  $\hat{O}_2$  can create vortices in the system. As mentioned earlier, if we flip the sign of the eigenvalue of the vortex operator at  $p$ , a vortex will be created in the system. Looking back at Equ.35, we see that the vortex configuration  $\{W_p\}$  is created by fixing the gauge at every link  $\{u_{ij}\}$ . Therefore, by changing the link operators, we can move between vortex sectors. Starting from a vortex-free sector with all link operators being +1, applying  $\hat{O}_1$  on site  $a$  will leave the  $\sigma_a^z$  untouched while flipping the  $\sigma_a^x$  and  $\sigma_a^y$ . Consequently, this will change the sign of the eigenvalue of the  $u_{ij}$  for x-link and y-link attached to site  $a$ , leaving the system with  $B_{p_1} = -1$  and  $B_{p_2} = -1$ . We can also move the vortices around in the system, by consecutively applying these operators on the particular sites in a path for which we want to move the vortices along. As an example, the red path shown in the Fig.6 corresponds to the operator

$$\hat{O} = \exp(-i\frac{\pi}{2}\sigma_i^z) \exp(-i\frac{\pi}{2}\sigma_j^x) \quad (38)$$

In general, we can define string operators to move the vortices anywhere in the system along the string, similar to the example above. To create such a string operator is straightforward now. If the string passes through a link, we need to apply an operator on one of the sites connected to that  $\alpha$ -link which carries  $\sigma^\alpha$  in the exponent. Before continuing, we need to make a convention. A sharp reader might point out that applying the operator  $\hat{O}' = \exp(-i\frac{\pi}{2}\sigma_l^z) \exp(-i\frac{\pi}{2}\sigma_k^x)$  instead of  $\hat{O}$  creates the same pair of vortices in the system. For consistency reasons, we therefore use the convention that if a string is passing through a link, the corresponding string operator is built up by picking the even site on the link. Having said all of this, a generic string operator is defined as

$$\hat{S} = \prod_{\alpha\text{-links}} \exp(-i\frac{\pi}{2}\hat{\sigma}_\alpha^\alpha) . \quad (39)$$

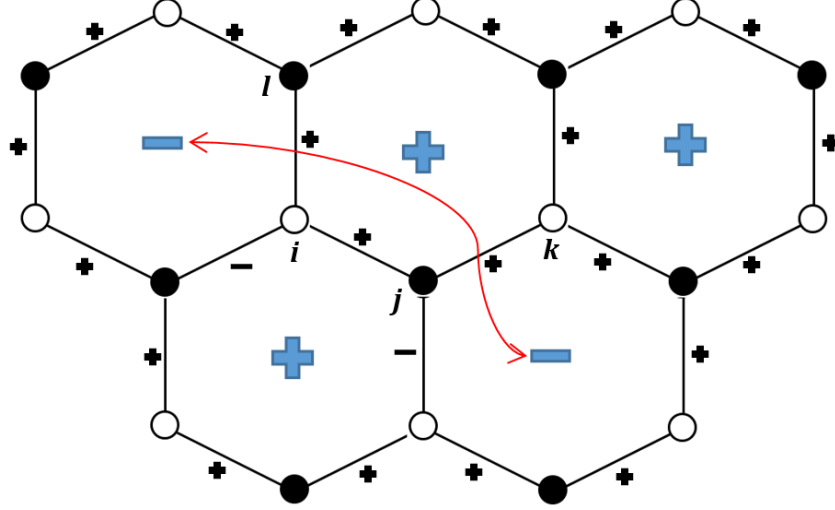


Figure 6: Two vortices connected by a string operator passing through several links. The white dots denote even lattice sites while the black dots are odd ones. By convention, the string operator is built up from operators acting on even sites.

This string operator will create two vortices at the ending points of the string which passes through the  $\alpha$  - links. The manipulation of link operators using these string operators is practically equivalent to changing the sign of the couplings  $J_{ij}$  corresponding to the link  $u_{ij}$  in the definition of the  $A_{ij}$  (see Equ.33). Therefore, in the RBM language one can simply redefine the Hamiltonian with the desired signs of  $J_{ij}$  for a particular vortex sector and then try to find the RBM representation for this new Hamiltonian through the approach explained in Section 3. The only practical disadvantage of this vortex realization approach is that it is computationally expensive as the RBM should be trained again from scratch to find the representation for the excited state. An ideal approach is one where, given the representation for the groundstate, we would be able to directly and without further optimization steps find the representation for the excited state.

In principle, it is possible to directly manipulate the weight and bias parameters of the RBM,  $\Omega = (a_k, b_{k'}, W_{kk'})$  to realize the vortices and find the excited state representation. Looking at Equ.22, we notice that there is a symmetry between the eigenvalues of physical spins and the value of parameters of the RBM. In other words, flipping a particular spin in site  $k$  is equivalent to flipping the sign of the RBM parameter sitting next to the  $\sigma_k^\alpha$  in Equ.22 and/or adding a phase to it. In general, for a string operator  $\hat{S}_l^\alpha = \exp(-i\frac{\pi}{2}\hat{\sigma}_l^\alpha)$  we have:

$$\begin{aligned} \hat{S} |\Phi\rangle &= (-i\hat{\sigma}_l^\alpha) \sum_{\Xi} \Phi_M(\Xi; \Omega) |\Xi\rangle \\ &= \sum_{\Xi} e^{[(-1)^{\delta(\alpha-z)-1} a_l] \sigma_l^z + \sum_{k \neq l} a_k \sigma_k^z} \times \\ &\quad \prod_{k'} \cosh \left( (-1)^{\delta(\alpha-z)-1} W_{lk'} \sigma_l^z + \sum_{k \neq l} W_{kk'} \sigma_k^z + b_{k'} \right) (-i\hat{\sigma}_l^\alpha) |\Xi\rangle. \end{aligned} \quad (40)$$

Next, one needs to evaluate how  $(-i\hat{\sigma}_l^\alpha)$  acts on  $|\Xi\rangle$ . Here we subdivide the three cases  $\alpha = z, x$  and  $y$ . If  $\alpha = z$ , spin up states will get a phase  $-i$  and spin down states a phase  $i$ . The overall effect of this can be absorbed in a shift of  $a_l$  by  $-i\frac{\pi}{2}$ . If  $\alpha = x$ , then spins up and down are just exchanged and the  $-i$  is an overall phase which can be ignored. If  $\alpha = y$ , we get a combination of the previous two cases.

$$\begin{aligned} \hat{S}_l^z : (W_{lk'}, a_l) &\mapsto (W_{lk'}, a_l - i\frac{\pi}{2}) \\ \hat{S}_l^x : (W_{lk'}, a_l) &\mapsto (-W_{lk'}, -a_l) \\ \hat{S}_l^y : (W_{lk'}, a_l) &\mapsto (-W_{lk'}, -a_l - i\frac{\pi}{2}). \end{aligned} \quad (41)$$

## 5 Results and Discussion

### 5.1 Groundstate

In this section, we present the results for the groundstate energy estimate of different system sizes for the proposed mapping discussed in Section 3. These results are also compared to the exact analytical expression given in Equ. 20. The absolute value of the energies is plotted in Fig. 7. All results for this and the following sections are for the *non-Abelian* phase  $J_x = J_y = J_z = 1$ .

The RBM has a simple fully-connected and two-layered architecture. The optimized value for the density of hidden nodes was found to be  $\alpha = \frac{num_h}{num_v} = 2$ . For lower values of  $\alpha$ , the network does not give an accurate estimate of energies, while the larger values cause over-fitting and again lead to inaccurate results. For training, the configuration space of the network has been sampled for hundreds of times, depending on the lattice size, using the Metropolis algorithm. Moreover, the stochastic gradient descent algorithm has been used for optimization using a suitable number of iterations such that the network converges to a low enough minimum of the energy landscape.

lattice size	$2 \times 2$	$2 \times 3$	$2 \times 4$	$3 \times 3$	$3 \times 4$	$4 \times 4$	$5 \times 5$	$6 \times 6$	$7 \times 7$
a.i	-6.4721	-9.8003	-12.5851	-14.2915	-18.9869	-25.1282	-39.3892	-56.7529	-77.1249
a.ii	-6	-9.2915	-12.4721	-14.2915	-19.0918	-25.4164	-39.3892	-56.2668	-77.1249
b	-6	-9.2915	-12.4721	-14.2915	-19.0918	-25.4164	-39.3892	-56.2668	-77.1249
c	-6.9282	-9.8003	-12.9443	-14.2915	-19.0918	-	-	-	-
d	-6.7197	-9.5414	-12.573	-13.7374	-18.0466	-24.0783	-37.305	-52.920	-71.793

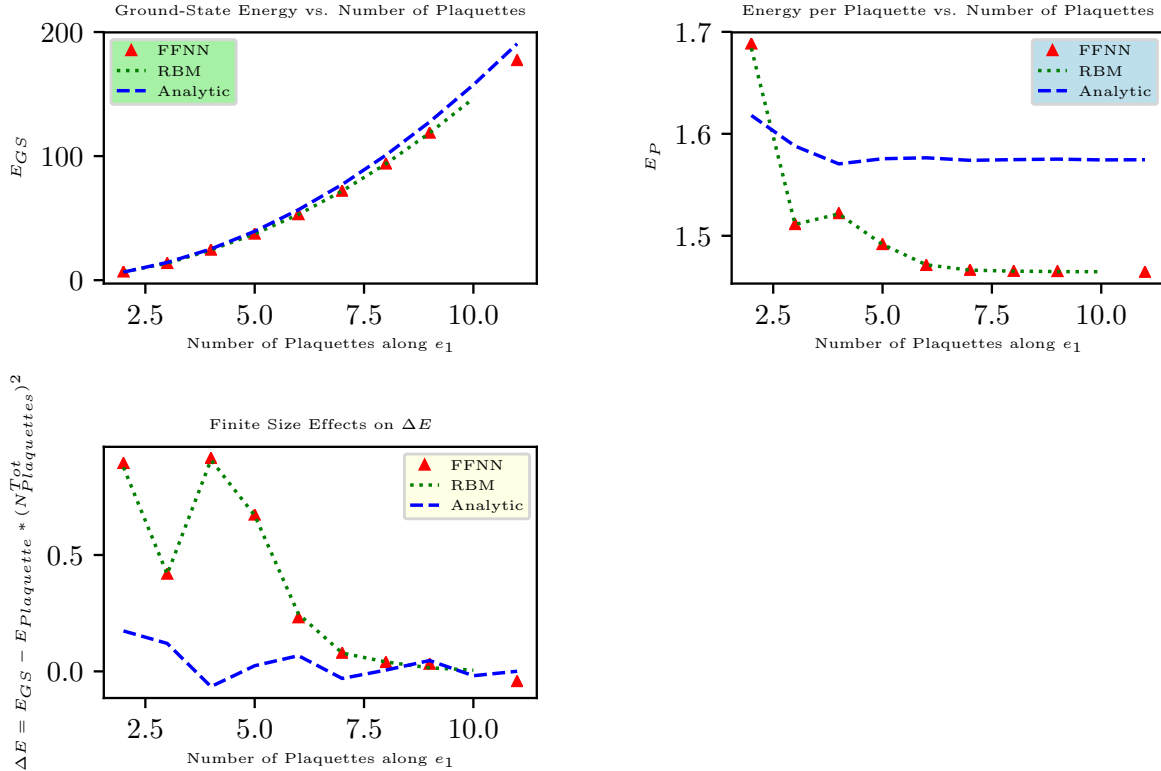


Figure 7: Numerical results for groundstate energy calculation using Restricted Boltzmann Machines (RBM) and Feed-Forward Neural Networks (FFNN) compared to the analytically obtained exact groundstate energy using Equ. 19.

The numerical results obtained are shown in Fig.7. The different methods for computing the groundstate energy listed in the table are as follows:

- a) Analytic formula Equ.20 using
  - i. anti-periodic boundary conditions
  - ii. periodic boundary conditions
- b) The method used by Kitaev and Pachos [2, 8]
- c) Direct diagonalization for small system sizes, using NetKet.
- d) RBM results for an architecture with  $\alpha = 2$  and 1k samples and 10k iteration steps.

Based on the results obtained for the energy of the groundstate of the system, training of the network was tested and optimized by changing the learning rate for different training phases and iteration numbers. However, the outcome did not considerably change or improve and it seems that the above results are the most accurate results one can get for this particular network architecture. We will later elaborate more on the reasons behind this discrepancy observed between the energy obtained using RBM and the analytical exact values.

In order to check the effect of the relative number of hidden and visible nodes on the outcome of the network, different values for  $\alpha$  were tested, keeping other parameters fixed. The  $\alpha$  parameter was changed just by changing the number of hidden nodes for a fixed system size (and hence fixed visible layer size) and the results are outlined in the table below, including the number of free parameters of the network. In order to keep things simple, we focus on one particular system size. The results summarized in the table are for a  $5 \times 5$  plaquette lattice with exact analytic energy being  $-39.3892$ .

$\alpha$	Number of Hidden Nodes	Number of Parameters	Energy
0.1	5	305	-27.7808(59)
0.3	15	815	-33.4312(37)
0.5	25	1325	-36.6024(22)
1.0	50	2600	-37.2464(13)
1.5	75	3875	-37.1235(15)
2.0	100	5150	-37.3054(14)
3.0	150	7700	-37.3037(14)
4.0	200	10250	-37.1007(16)
6.0	300	15350	-37.2989(14)
8.0	400	20450	-37.1710(15)
10.0	500	25550	-37.1946(15)

Table 1: Numerical results for the density of hidden nodes,  $\alpha = \frac{num_h}{num_v}$ , and its influence on groundstate energy calculation.

### The performance of FFNN vs. no-visible-bias RBM

In Table 2, we give a brief summary of the comparison results between an FFNN with one layer and a no-visible-bias RBM (referred to as novb-RBM in the table). The two architectures are similar and for the same computational resources (such as CPU and memory) and system size these results have been obtained.

$\alpha$	# Hidden Nodes	# Parameters	Energy(FFNN)	Energy(novb-RBM)	Time(FFNN)	Time(novb-RBM)
1.0	50	2550	-37.2401(15)	-37.1532(15)	2783s	2754s
2.0	100	5100	-37.2958(14)	-36.8954(18)	4591s	5476s
3.0	150	7650	-37.3007(14)	-37.2191(15)	6889s	8331s

Table 2: Comparison between a single-layer FFNN and a novb-RBM performance, in terms of training time and accuracy of energy for a  $5 \times 5$  plaquette lattice.

The conclusion we reach is:

1. The FFNN trains faster than the RBM with relatively fewer free parameters and performs better than the RBM with no bias.

2. But the FFNN's result again deviates by a similar margin from the analytic result.

One explanation for the slight deviation of the RBM result from the exact analytic result is that the RBM result is not in an exact eigenstate of the plaquette operators  $W_p$ . In fact, we find that the sum of all plaquette operator expectation values is close to zero, whereas the true groundstate should have  $W_p = +1$  for all plaquettes  $p$ . Thus the state we are finding seems to be a highly entangled state composed of the true groundstate as well as certain excited states with small energy. This seems to be a side effect of the gradient descent algorithm for minimizing the energy expectation value. We will have more to say about how to circumvent this constraint in Section 5.3.

## 5.2 Creating Vortex pairs and measuring their energy

As described in Section 4, there are three theoretically equivalent methods to create vortices:

- (a) modifying parameters of RBM
- (b) creating an auxiliary Hamiltonian and training it again
- (c) transforming into auxiliary fermion representation and fixing  $u_{ij}$ s [2, 8]

We applied all three methods to a  $3 \times 3$  lattice and computed the corresponding energy levels for excited states. The numerical result obtained for the groundstate energy of a  $3 \times 3$  lattice is  $-13.7166(2)$ , while the theoretical groundstate energy is  $-14.2915$ . For excited states obtained by flipping spins, the results we get are shown in the table below.

Spins Flipped	Energy(Method A)	Energy(Method B)	Energy(Method C)
$\sigma_8^y$	-11.7335(5)	-12.1070(51)	-13.9146
$\sigma_9^y$	-11.7474(5)	-11.8873(57)	-13.9146
$\sigma_8^x \sigma_8^z$	unrealizable	-12.7447(37)	-13.9146

Table 3: Energy of excited states with a pair of vortices in a  $3 \times 3$  lattice system, measured through different methods as explained in the text.

We find that method (a) is more stable than method (b), which might be due to the random initialization of RBM parameters in method (b) for the training process. Both methods, (a) and (b), deviate by a margin from the analytic values, namely method (c). This can be again explained by the fact that the state from which these states are obtained by flipping, is not a true groundstate but an entangled state. This can be confirmed by measuring the plaquette operators in the excited states we created and the result is again a value close to zero rather than  $+1$  or  $-1$ .

## 5.3 Quantum State Tomography for Groundstate

In this section we apply the technique discussed in Section 3.2 to reconstruct the wave function from measurements. In order to generate measurement data set, we sample from an exact groundstate by random measurements in different basis. To this end, we focus on the  $2 \times 2$  lattice in order to deal with the computational resource requests and also being able to find the exact groundstate wave function through exact diagonalization. The last step is to train the RBM using the data set obtained. The result is shown in Fig. 8.

There are many intricate parameters which one can adjust during training, such as learning rate, batch size, number of Metropolis samples, and number of single measurements. Only with a suitable choice of parameters and large enough training data set, can one achieve a satisfactory result. For the example depicted in Fig. 8, in order to build the training data set, the exact wave function was sampled 2000 times for 256 randomly chosen basis  $x, y, z$  and the hidden node density  $\alpha$  was set equal to 2. With this combinations of parameters, QST leads to an overlap of 97 percent between the exact wave function and the learned one.

### Plaquette Operator expectation values and spin flipping

Starting from the state obtained from tomography as discussed above, one can then realize vortices in the system by modifying parameters of the RBM as described in Section 4. In order to verify that modification of RBM parameters takes us to the right excited state, we measure the relevant plaquette operators in the system. The convention for labeling plaquette operators and sites is as shown in Fig. 9.

For the trained RBM state after performing QST for groundstate of  $2 \times 2$  lattice, the expectation values of its four plaquette operators as well as the measured energies are shown in Table 4. Moreover, flipping the  $y$ - and  $z$ -components of the spin at lattice site number 5 (or equivalently, applying  $\hat{S}_5^x$ ) will produce a pair of vortices at  $B$  and  $D$  plaquettes.

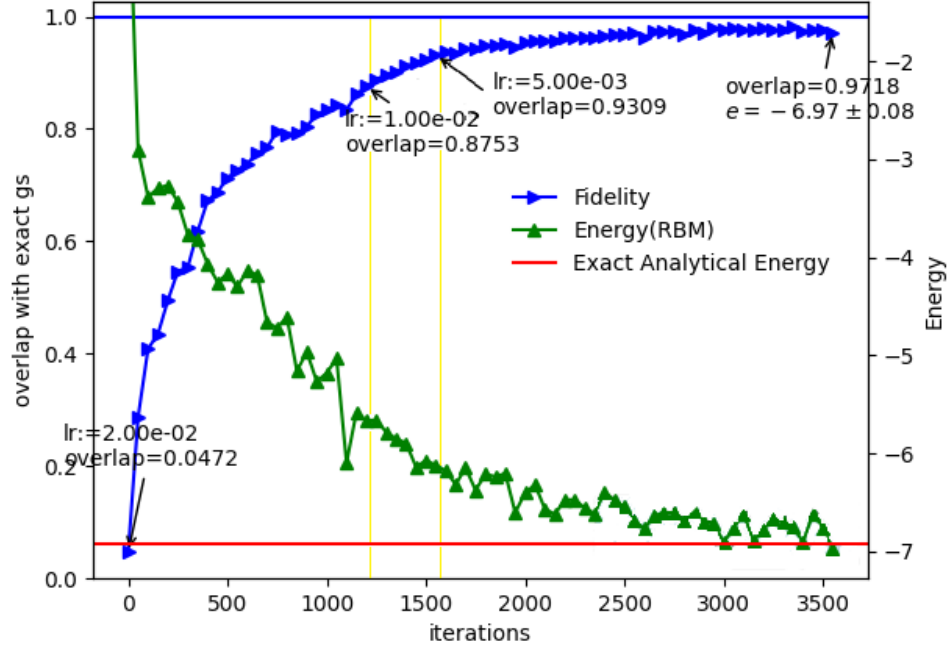


Figure 8: Energy and overlap results for QST of  $2 \times 2$  lattice system for different training phases with specified learning rates in the figure.

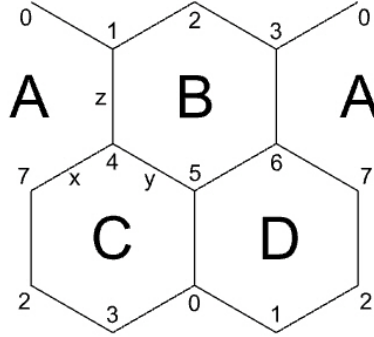


Figure 9: Labeling convention for plaquette operator measurements.

Therefore, the expectation value of the  $\hat{W}_p$  operator in these plaquettes also flips sign. Similarly, applying  $\hat{S}_7^y$ , will kill the vortex in plaquette  $D$  and produce one in plaquette  $A$ . The changes in the sign of expectation values for these plaquettes is shown in the Table 4 below. Finally, by applying  $\hat{S}_3^z$  we return back to the no-vortex sector. These results, prove the effectiveness of the framework developed in Section 4 for realization of vortices in RBM states, in both QST and usual learning approaches.

Note that the energy after each flip changes by an amount  $\Delta E \sim 2$ . This can be explained by the fact that each vortex sector has its own groundstate but also excited states with higher energies created by fermionic quasi-particle excitations. For example, the no-vortex sector has a spectrum given by the Hamiltonian in Equ. 20 and while the



Spin Flip Operator (acting successively)	$W_A$	$W_B$	$W_C$	$W_D$	Energy
Groundstate	0.94889473	0.95168581	0.95248031	0.95528330	-6.0778
$\hat{S}_5^x$	0.94889473	-0.95168581	0.95248031	-0.95528330	-4.0105
$\hat{S}_7^y$	-0.94889473	-0.95168581	0.95248031	0.95528330	-1.8040
$\hat{S}_3^z$	0.94889473	0.95168581	0.95248031	0.95528330	0.0606

Table 4: Expectation values of plaquette operators after applying a series of spin flip operators on the RBM state obtained from QST.

groundstate is the lowest lying state in this sector, there will be excited quasi-particle states carrying momentum  $\mathbf{k}$  which are created by the  $\gamma_{\mathbf{k}}^\dagger$  operators. Similarly, vortex sectors with a non-trivial vortex number can be in an excited state by applying quasi-particle creation operators. A rough estimate shows that the difference  $\Delta E \sim 2$  is of the order of such a quasi-particle excitation and thus the vortices we are creating carry such excitations. This also explains why when returning to the no-vortex sector we do not arrive at the original energy.

## 6 Conclusion

In this paper we have constructed RBM realizations of several sectors of the Kitaev Honeycomb model. In particular, we have focused on the gap-less non-Abelian phase corresponding to the parameter choice  $J_x = J_y = J_z$  and used machine learning algorithms to train restricted Boltzmann machines in order to find groundstates and excited states of such systems. We find that one can achieve a groundstate realization to a reasonable approximation and also realize excited states. Moreover, using quantum state tomography we have been able to reconstruct an exact wavefunction from single shot measurements and used this method to “detect” the vortex state of the system. This is useful for applications in topological quantum computation where one would need to “decode” input data, then perform a quantum gate operation, and finally create an output.

Of course, in the case of the Honeycomb model we have an exact solution of the spectrum using Kitaev’s Majorana fermion representation. However, such a representation, though giving exact values for the energies of given states in the Hilbert space, is at the same time losing information. For example it is difficult and in some cases unknown how to compute expectation values of string operators composed of Pauli matrices. Moreover, one may lose the Majorana representation in cases where a complicated perturbation is added to the Hamiltonian which obscures such a simple representation. For all these reasons it is desirable to obtain realizations of the quantum state in terms of spin eigenstates and the RBM given in Equ.21 is such a representation. It would be interesting to look at further refinements of the RBM representation which would allow us to find more accurate approximations of ground and excited states as well as shorter learning times. One way to achieve this is to use “projected gradient descent” where after each learning step/gradient step one projects the parameters of the RBM to a subspace corresponding to a specific vortex sector of the physical system. We leave such refinements and further applications for future work.

The software framework developed for this project is publicly available at <https://github.com/mrnp95/TQC/>.

## 7 Acknowledgement

MN would like to thank Yau Mathematical Science Center (YMSC) for hospitality during the early stages of this work. He also thanks Martin Duy Tat for helpful discussions. The work of BH and YS is supported by the National Thousand-Young-Talents Program of China. BH would also like to thank the Bethe Center for Theoretical Physics in Bonn, where part of this work was completed, for hospitality. Part of the numerical calculations were performed on the SARMA computing cluster at Shahid Beheshti University but the majority of the work was done using the Spinor cluster at YMSC.

## References

- [1] A. Kitaev, *Anyons in an exactly solved model and beyond*, *Annals of Physics* **321** (2006) .
- [2] A. Kitaev, *Fault-tolerant quantum computation by anyons*, *Annals of Physics* **303** (2003) .
- [3] G. Jackeli and G. Khaliullin, *Mott insulators in the strong spin-orbit coupling limit: From heisenberg to a quantum compass and kitaev models*, *Physical Review Letters* **102** (2009) .

- [4] K. S. Tikhonov, M. V. Feigelman and A. Y. Kitaev, *Power-law spin correlations in a perturbed spin model on a honeycomb lattice*, *Physical Review Letters* **106** (2011) .
- [5] D.-L. Deng, X. Li and S. Das Sarma, *Machine learning topological states*, *Physical Review B* **96** (2017) .
- [6] G. Carleo, K. Choo, D. Hofmann, J. E. T. Smith, T. Westerhout, F. Alet et al., *Netket: A machine learning toolkit for many-body quantum systems*, *SoftwareX* (2019) .
- [7] G. Torlai, G. Mazzola, J. Carrasquilla, M. Troyer, R. Melko and G. Carleo, *Neural-network quantum state tomography*, *Nature Physics* **14** (2018) .
- [8] J. K. Pachos, *Introduction to Topological Quantum Computation*. Cambridge University Press, 2012, 10.1017/CBO9780511792908.
- [9] P. Schollm and R. Orus, *Kitaev honeycomb tensor networks: Exact unitary circuits and applications*, *Physical Review B* **95** (2017) .
- [10] P. Jordan and E. P. Wigner, *About the Pauli exclusion principle*, *Z. Phys.* **47** (1928) .
- [11] H.-D. Chen and Z. Nussinov, *Exact results of the kitaev model on a hexagonal lattice: spin states, string and brane correlators, and anyonic excitations*, *Journal of Physics A: Mathematical and Theoretical* **41** (2008) .
- [12] E. H. Lieb, *Flux phase of the half-filled band*, *Physical Review Letters* **73** (1994) .
- [13] N. Le Roux and Y. Bengio, *Representational power of restricted boltzmann machines and deep belief networks*, *Neural Computation* **20** (2008) .
- [14] D. W. Zhang, Y. Q. Zhu, Y. X. Zhao, H. Yan and S. L. Zhu, *Topological quantum matter with cold atoms*, *Advances in Physics* **67** (2018) .
- [15] C. Nayak, S. H. Simon, A. Stern, M. Freedman and S. Das Sarma, *Non-abelian anyons and topological quantum computation*, *Reviews of Modern Physics* **80** (2008) .
- [16] A. J. Leggett, *Lecture 26, the kitaev models*, **PHYS598PTD**, University of Illinois, Department of Physics (2013) .
- [17] F. L. Pedrocchi, S. Chesi and D. Loss, *Physical solutions of the kitaev honeycomb model*, *Physical Review B* **84** (2011) .